


Functional renormalization group for fermion lattice models in three dimensions: Application to the Hubbard model on the cubic lattice

J. Ehrlich ^{*}

*Institute for Theoretical Solid State Physics, RWTH Aachen University, 52056 Aachen, Germany
and Peter Grünberg Institute and Institute for Advances Simulation, Forschungszentrum Jülich, 52428 Jülich, Germany*

C. Honerkamp 

*Institute for Theoretical Solid State Physics, RWTH Aachen University, 52056 Aachen, Germany
and Jülich-Aachen Research Alliance-Fundamentals of Future Information Technology, Aachen, Germany*



(Received 4 May 2020; revised 2 October 2020; accepted 2 October 2020; published 5 November 2020)

The channel-decomposed functional renormalization group (FRG) approach, most recently presented in the variant of truncated-unity FRG (TUFRG), has so far been used for various two-dimensional model systems. Yet for many interesting material systems the third spatial dimension is of clear relevance. Therefore, FRG schemes working in three spatial dimensions (3D) are definitely on the wish list. Here we demonstrate that a 3D TUFRG scheme can be set up in a straightforward extension of previous two-dimensional codes and gives physically sensible results with affordable numerical effort, regarding both the qualitative and quantitative descriptions. The computed phase diagram of the three-dimensional Hubbard model at half filling or perfect nesting shows a phase transition to a (π, π, π) -ordered antiferromagnetic ground state for repulsive interactions at an energy scale that compares well with other numerical approaches in the literature. Furthermore, the method allowed us to detect a d -wave pairing and a concurring $(\pi, \pi, 0)$ antiferromagnetic ground state in the hole-doped Hubbard model.

DOI: [10.1103/PhysRevB.102.195108](https://doi.org/10.1103/PhysRevB.102.195108)

I. INTRODUCTION

Quantum materials with significant correlation effects arising from the interactions within the electron system are under intense experimental and theoretical study, as they give rise to a plethora of interesting phases like magnetic orderings and unconventional superconductivity, with potential uses in future technologies. One of the simplest lattice models leading to correlation effects is the single-band Hubbard model, where electrons interact via a repulsive coupling U with each other only when they are located at the same lattice site. Despite its simplicity, analytic solutions of this model for $U \neq 0$ exist only in single cases and limits like in the limit of one [1] or infinite dimensions [2] for regular n -dimensional cubic lattices.

The Hubbard model exhibits in the case of three spatial dimensions and half-filling a transition to an antiferromagnetic (AFM) ordered ground state for all interaction strengths U at finite Néel temperatures T_N . This T_N depends on the interaction strength U , as the transition is attributed to different effects: In the weak-interaction limit it is caused by thermal spin-flip excitations across the Fermi surface, which can be described reasonably well by the random-phase approximation (RPA) extended by corrections due to local quantum fluctuations [3–5]. In this weak-coupling case the self-consistent perturbation theory allows us to derive

an analytic $T_N(U)$ curve [6]. In the strong-coupling case the phase transition is caused by spin-spin interactions of local moments. Thus, the Hubbard model converts to the Heisenberg model with $J = t^2/U$, and the Néel temperature tends to the Heisenberg limit $3.83/U$ [7,8]. In this limit, when the interaction reaches the order of the bandwidth, a Mott-insulator transition can be detected above the magnetic ordering temperature [9], maintaining an excitation gap for the magnetically disordered phase at larger U .

As the $T_N(U)$ curve grows from these limiting cases towards intermediate coupling strength, it is expected to exhibit a maximum in this region, which was shown to go along a pseudogaplike behavior [10]. But as an analytic solution exists only for $U \rightarrow 0$, the exact form of $T_N(U)$ has been targeted by numerous methods [9,11–14]. Therefore, the Néel curve $T_N(U)$ of the three-dimensional half-filled Hubbard model can be used as a reference for new methods.

In addition to this specific case, the three-dimensional Hubbard model has been extended and studied in different specific aspects. With an additional next-nearest-neighbor hopping t' , the magnetic order is reduced due to magnetic frustration [10]. An extension of the Hubbard model by nearest-neighbor interactions leads to a rich phase diagram containing different magnetic orders, charge and spin density waves, and superconductivity, depending on the strength of the interactions [15,16]. The simplest way, doping the system away from half-filling, showed that d -wave pairing can become dominant [17]. This richness of phases occurring for sometimes already small detunings away from perfect nesting makes it important

*j.ehrlich@fz-juelich.de

to treat all contributions to correlation effects on the same footing.

The functional renormalization group (FRG) appears to be a suitable method in this regard, as it treats all three channels (spin, charge, and pairing) on the same footing. Although the FRG is well established for investigations in one- or two-dimensional correlated systems [18–20], it has not been applied to lattice systems in three dimensions so far due to numerical costs of the most often used N -patch Brillouin zone discretization scheme. In recent years, however, channel-decomposition techniques in conjunction with form-factor expansions have defined a new and powerful FRG line of approach [21–27]. In contrast to the N -patch schemes, a much higher momentum resolution can be reached in the new schemes [26,28], and various other improvements like a detailed frequency dependence of the interactions [29,30] could be built in. Most notably, in a recent study, multiloop corrections were incorporated and shown to converge for the two-dimensional (2D) Hubbard model at perfect nesting [31]. Thus, the method can be understood to be quantitatively reliable, at least for simple situations. A neat way to derive the FRG equations in this FRG approach is the insertion of truncated resolutions of unity into the loop diagrams. This allows us to cast the flow equations for the interaction vertex in the form of matrix products which can be parallelized efficiently. This technique is known as truncated-unity FRG (TUFGR [26]) and will be employed in what follows. On the level used here, the TUFGR can be viewed as a reformulation of the singular mode FRG by Wang *et al.* [24,25].

The numerical cost of the TUFGR scales quadratically in the number of Brillouin zone (BZ) points taken into account and quartically with the number of form factors kept. If we now extend the scheme from two to three dimensions while requesting the same momentum resolution of n_{kpt} points in each spatial direction, the total number of points in the BZ increases from n_{kpt}^2 to n_{kpt}^3 , but this may still be tolerable if we do not need ultrahigh precision. The number of form factors, however, increases but remains comparable, thus making a treatment of three-dimensional models by TUFGR possible. In this paper we, therefore, apply it to the three-dimensional Hubbard model while neglecting the self-energy flow (which can be built in in subsequent works along the lines of Refs. [31,32]). By this we reproduce the weak-coupling part of the AFM phase diagram and find d -wave pairing regimes in the doped three-dimensional Hubbard model.

This paper is organized as follows. In Sec. II we briefly introduce the truncated-unity functional renormalization group equations and describe their implementation as well as the model in Sec. III. In Sec. IV A we discuss the phase diagram, and in Sec. IV B we show the arising d -wave pairing when doping the Hubbard model, before we conclude in Sec. V.

II. METHOD

The TUFGR, which we use here, is a recently developed [26] efficient approximation of the FRG and, by now, a well-established tool for the investigation of two-dimensional correlated systems [19,31,32]. The basic idea of the one-particle irreducible (1-PI) FRG is to introduce a dependence on a scale parameter Λ to the noninteracting Green's function.

Variation of Λ induces a flow of correlation and vertex functions of the system. A typical choice is to implement the scale parameter Λ as an infrared energy or frequency cutoff, such that only modes with an absolute value of the band energy or a Matsubara frequency larger than the cutoff are considered. Below we actually apply a smoothed frequency cutoff function first employed by Husemann and Salmhofer [21]. In any case, in the limit $\Lambda \rightarrow 0$ the full system is obtained again. An infinite set of differential flow equations for the effective, Λ -dependent n -particle interactions can be derived by the Λ derivative of the corresponding generating functional [19,33]. For the case of weak to intermediate interactions, it is usually assumed that it is sufficient to neglect interactions of order larger than $n \geq 3$, drastically simplifying the calculations [33]. Note that recently, so-called multiloop extensions were implemented in the FRG [31,34]. These allow one to reduce the error from this truncation to such a degree that equivalence to the parquet approximation is obtained, resulting in good quantitative agreement [32].

In the general form, the flow equation for the two-particle interaction contains contributions of the particle-particle (pp), the crossed particle-hole (ph,cr), and the direct particle-hole (ph,d) channels, which represent all possible topologically nonequivalent combinations of two vertices connected by a full Green's function G^Λ and a single scale propagator $S^\Lambda = -G^\Lambda (\frac{d}{d\Lambda} G_0^\Lambda) G^\Lambda$. As the Hubbard model is SU(2) symmetric and a spontaneous symmetry breaking is only allowed to be approached but not to occur in the present paper, we employ the SU(2)-symmetric form of the FRG equations as, e.g., in Ref. [19]. By this choice, it is sufficient to consider the spin-independent vertex V . When the decomposition of the full interaction into V is inserted and the inner spin summation is performed, the pairing and crossing particle-hole channels still consist of one diagram, while the direct particle-hole channel consists of three contributions (see Fig. 1). Besides exploiting the SU(2) symmetry, we further simplify the calculations by neglecting self-energy corrections, such that our main element of interest is the 1-PI interacting vertex V depending on four momenta, frequencies, and orbitals or bands. Exploiting energy and momentum conservation within the vertex reduces the number of frequency and momentum arguments by one. The numerical effort scales with the fourth order in frequencies and momenta due to the external legs and the internal loop summation, such that an investigation with high resolution is limited by both memory and computing time. This limitation can be overcome for the momentum part by the TUFGR, which builds on earlier ideas of channel decomposition and form-factor expansion [21,22] and represents a reformulation of the singular-mode FRG by Wang *et al.* [24,25].

In the following we sketch the main elements of the TUFGR. For more details, see Refs. [26,27,31]. In a first step, the full flowing interaction vertex can be split into four parts, corresponding to the initial interaction and the three channels. We write

$$\begin{aligned} V^\Lambda(\mathbf{k}_1, \mathbf{k}_2; \mathbf{k}_3) &= V_0(\mathbf{k}_1, \mathbf{k}_2; \mathbf{k}_3) - \Phi^{\Lambda, \text{P}}(\mathbf{k}_1 + \mathbf{k}_2; \mathbf{k}_1, \mathbf{k}_3) \\ &\quad + \Phi^{\Lambda, \text{C}}(\mathbf{k}_3 - \mathbf{k}_2; \mathbf{k}_1, \mathbf{k}_3) + \Phi^{\Lambda, \text{D}}(\mathbf{k}_1 - \mathbf{k}_3; \mathbf{k}_1, \mathbf{k}_4). \end{aligned} \quad (1)$$

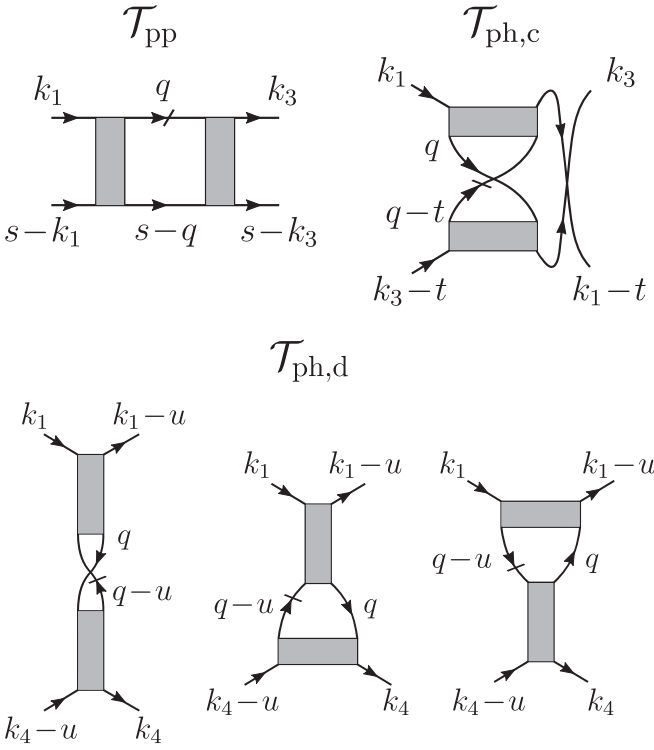


FIG. 1. Diagrammatic representation of the SU(2)-symmetric, 1-PI functional RG interaction at one-loop truncation, representing the particle-particle (\mathcal{T}_{pp}), crossing ($\mathcal{T}_{ph,c}$), and direct ($\mathcal{T}_{ph,d}$) particle-hole contributions. The momenta are provided in the channels' natural representation with three independent momenta, as provided by Eq. (2).

Each channel $\Phi^{\Lambda,X}$ with $X = P, C, D$ has a characteristic main total momentum or transfer

$$\begin{aligned} s &\equiv k_1 + k_2 && (\text{pp}), \\ t &\equiv k_1 - k_4 && (\text{ph,cr}), \\ u &\equiv k_1 - k_3 && (\text{ph,d}) \end{aligned} \quad (2)$$

as the first argument. From general arguments and previous calculations (see, e.g., Ref. [19] and references therein), a strong dependence on s , t , or u is known to show up in the full vertex if spontaneous symmetry breaking corresponding to this channel is approached at low scales. For the FRG flow, each $\Phi^{\Lambda,X}$'s Λ derivative is taken to be the corresponding diagrams \mathcal{T}^X in Fig. 1, which also depend strongly on one of the characteristic momenta s , t , and u . Besides the strong dependence on s , t , or u , the channel couplings $\Phi^{\Lambda,X}$ are found to only weakly depend on their second and third arguments. Thus, the weak dependencies can be described [26] by a small number of slowly varying basis functions in the Brillouin zone, called form factors. Therefore, in a second step, the weak dependencies are projected to a form-factor basis $\{f_i\}$, and we call the projections of the $\Phi^{\Lambda,X}$ to this basis the propagator of the X channel, denoted by $P_{m,n}^{\Lambda}(s)$, $C_{m,n}^{\Lambda}(u)$, and $D_{m,n}^{\Lambda}(t)$. By this procedure each channel propagator has its

own flow equation,

$$\begin{aligned} \dot{P}_{m,n}^{\Lambda}(s) &= V_{m,i}^{\Lambda,P}(s) \chi_{i,j}^{\Lambda,pp}(s) V_{j,n}^{\Lambda,P}(s), \\ \dot{C}_{m,n}^{\Lambda}(u) &= V_{m,i}^{\Lambda,C}(u) \chi_{i,j}^{\Lambda,ph}(u) V_{j,n}^{\Lambda,C}(u), \\ \dot{D}_{m,n}^{\Lambda}(t) &= 2V_{m,i}^{\Lambda,D}(t) \chi_{i,j}^{\Lambda,ph}(t) V_{j,n}^{\Lambda,D}(t) \\ &\quad + V_{m,i}^{\Lambda,C}(t) \chi_{i,j}^{\Lambda,ph}(t) V_{j,n}^{\Lambda,D}(t) \\ &\quad + V_{m,i}^{\Lambda,D}(t) \chi_{i,j}^{\Lambda,ph}(t) V_{j,n}^{\Lambda,C}(t), \end{aligned} \quad (3)$$

where i and j are form-factor indices to be summed over. These equations are products of three matrices in the form-factor basis, scaling linearly with the number of momenta. The terms

$$\chi_{i,j}^{\Lambda,pp}(s) = \int \frac{dq}{(2\pi)^3} f_i^*(q) f_j(q) L_{pp}^{\Lambda}(q, s), \quad (4)$$

$$\chi_{i,j}^{\Lambda,ph}(t|u) = \int \frac{dq}{(2\pi)^3} f_i^*(q) f_j(q) L_{ph}^{\Lambda}(q, t|u)$$

are the projections of the particle-particle and particle-hole propagators to the form-factor basis. The dual propagators in the context of FRG are provided by

$$\begin{aligned} L_{pp}(q, s) &= S^{\Lambda}(q) G^{\Lambda}(s-q) + S^{\Lambda}(s-q) G^{\Lambda}(q), \\ L_{ph}(q, t) &= S^{\Lambda}(q) G^{\Lambda}(q-t) + S^{\Lambda}(q-t) G^{\Lambda}(q), \end{aligned} \quad (5)$$

in which G^{Λ} is the scale-dependent Green's function and S^{Λ} is the single-scale propagator $S^{\Lambda} = -G^{\Lambda}(G_0^{\Lambda})^{-1}G^{\Lambda}$. The terms $V_{i,j}^{\Lambda,X}$ are the projections of the full vertex to channel X, e.g.,

$$V_{i,j}^{\Lambda,P}(s) = \int \frac{dq}{(2\pi)^3} \int \frac{dq'}{(2\pi)^3} f_i^*(q) V^{\Lambda}(q, -q+s, q') f_j(q'). \quad (6)$$

Due to the decomposition of the full vertex V^{Λ} this requires the projection of the other propagators and the initial interaction to the corresponding channel. For example, projecting the C channel to the P channel becomes

$$\begin{aligned} \hat{P}[\Phi^C]_{m,n}(s) &= \int \frac{dq}{(-2\pi)^3} \frac{dq'}{(2\pi)^3} f_m^*(q) f_n(q') \\ &\quad \times \sum_{i,j} f_i(q) f_j^*(q') C_{i,j}(q+q'-s), \end{aligned} \quad (7)$$

where the back projection from the form factor to three-momentum space was used for the C-channel propagator. To conclude, in the TUFGRG we have to solve the propagator flow equations (3), which require a form-factor projection of the two-propagator term (4) and the channel-to-channel projections like the one in (7), which scales linearly with the number of momenta. For a further discussion of the formalism and additional aspects like self-energies, frequency dependence, multiloop extensions, and susceptibilities, see, e.g., Ref. [31].

III. MODEL AND IMPLEMENTATION DETAILS

In order to test the TUFGRG in three spatial dimensions, we investigate the isotropic one-band Hubbard model given by the Hamiltonian

$$\mathcal{H} = -t \sum_{(i,j),\sigma} c_{i,\sigma}^{\dagger} c_{j,\sigma} + U \sum_i n_{i\uparrow} n_{i\downarrow} \quad (8)$$

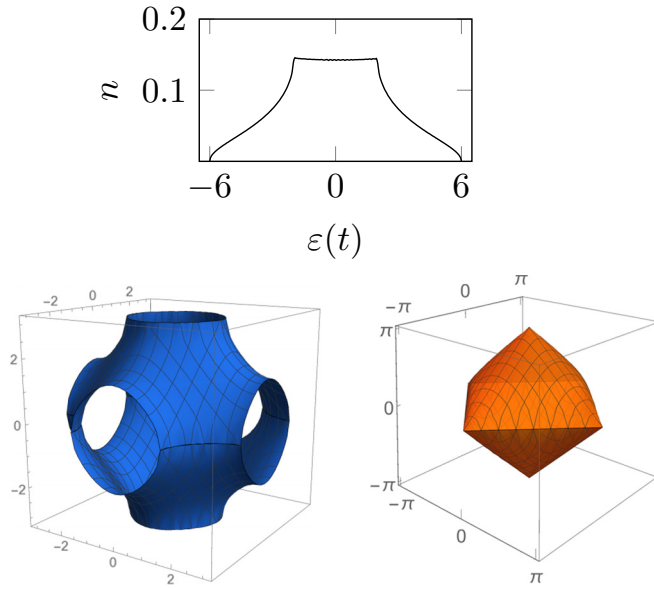


FIG. 2. The density of states (top) and the Fermi surfaces of the 3D Hubbard model at $\mu = 0t$ (bottom left) and $\mu = -2t$ (bottom right).

on a simple-cubic three-dimensional lattice. Here t denotes the hopping amplitude between nearest neighbors, and $c_{i,\sigma}^\dagger$ ($c_{i,\sigma}$) creates (annihilates) an electron with spin σ on site i . U is the on-site Coulomb interaction, and $n_{i,\sigma} = c_{i,\sigma}^\dagger c_{i,\sigma}$ is the particle density on site i . The noninteracting dispersion of the Hamiltonian given in (8) is

$$\varepsilon_{\mathbf{k}} = -2t[\cos(k_x) + \cos(k_y) + \cos(k_z)] - \mu. \quad (9)$$

The chemical potential μ is defined such that $\mu = 0$ holds for the half-filled system as self-energy corrections are not considered in this work. The corresponding density of states and Fermi surface for half-filling and for a smaller filling are shown in Fig. 2. We will use t as the energy unit from now on.

Although Eq. (8) may be one of the simplest possible interacting many-fermion Hamiltonians, it cannot be solved analytically. The main questions here concern the properties and energy scales of potentially ordered ground states. To obtain this information we use the TUFGR presented in Sec. II, given by Eqs. (3), (4), and (7) (with the other channels treated analogously). We start the flow equations at a high-energy cutoff of $\Lambda_0 = 30$ with an initial interaction $V_0 = U$ for all momentum combinations corresponding to the on-site Hubbard interaction. To obtain the pp- and ph-bubble terms χ we neglect self-energy effects; that is, the internal lines are bare Green's functions $G^\Lambda = G_0^\Lambda$ and single-scale propagators $S^\Lambda = \frac{d}{d\Lambda} G_0^\Lambda$.

In the FRG flow, we use a smooth frequency cutoff function [21] $C_\Lambda(\omega_n) = \frac{\Lambda^2}{\Lambda^2 + \omega_n^2}$ on the free Green's function G_0 whose derivative, therefore, is in the single-scale propagator S^Λ . As in many previous works, we use the static approximation with frequency-independent vertices. Then, at $T = 0$, the bubble terms in Eqs. (4) become (before momentum

TABLE I. List of form factors $f_i(\mathbf{k})$ used for the calculations, transforming according to irreducible representations of the cubic group O_h . For the phase diagram calculation only the first seven corresponding to on site and nearest neighbor were used, while for the doped system the full list including some second-nearest-neighbor form factors was used.

Name	Momentum space representation
s	const
extended s	$\cos(k_x) + \cos(k_y) + \cos(k_z)$
$d_{x^2-y^2}$	$\cos(k_x) - \cos(k_y)$
d_{z^2}	$-\cos(k_x) - \cos(k_y) + 2\cos(k_z)$
p_x	$\sin(k_x)$
p_y	$\sin(k_y)$
p_z	$\sin(k_z)$
s_3	$\cos(k_x)\cos(k_y) + \cos(k_x)\cos(k_z) + \cos(k_y)\cos(k_z)$
d_{xy}	$\sin(k_x)\sin(k_y)$
d_{xz}	$\sin(k_x)\sin(k_z)$
d_{yz}	$\sin(k_y)\sin(k_z)$

summation)

$$L_{\text{pp/ph}}^\Lambda(\mathbf{k}, \mathbf{k}') = \frac{d}{d\Lambda} \int_{-\infty}^{\infty} \frac{d\omega}{2\pi} \frac{\omega^2}{\omega^2 + \Lambda^2} \frac{1}{i\omega - \varepsilon_{\mathbf{k}}} \frac{\omega^2}{\omega^2 + \Lambda^2} \frac{1}{\mp i\omega' - \varepsilon_{\mathbf{k}'}} \quad (10)$$

where the frequency integral can be solved analytically.

In Eqs. (4) and (7) we use form factors $f_i(\mathbf{q})$ corresponding to the O_h symmetry group of the crystal lattice, representing bonds up to the second-nearest neighbors, as shown in Table I. As these form factors are sums of δ functions in real space, the channel-to-channel projections like the one in Eq. (7) are performed by transforming the right-hand side to real space, resulting in a combinatorial problem of multiplying real-space representations of the form factors, but without the need to perform two integrations over momentum space. For the calculations in Sec. IV A a regular momentum grid of 16^3 was used for the representation of the vertex, i.e., for the first entries in $\Phi^{P/C/D}$, while the bubbles as in Eq. (4) were evaluated on a 560^3 momentum mesh which we observed to give well-converged results over the full investigated range of U . As an antiferromagnetic state is expected, we considered only the on-site and nearest-neighbor form factors (the first seven in Table I). The FRG flow starts at the initial scale $\Lambda_0 = 30t$, which is well above the bandwidth, with an initially chosen Hubbard interaction U . Starting from this interaction, the full vertex evolves during integration of the cutoff scale and may become divergent. Therefore, the flow was stopped when the largest value of a propagator exceeded the maximum of $V_{\text{max}} = 50t$. The leading component in $\Phi^{P/C/D}$ is used to identify the type of emergent order that is signaled by this flow to strong coupling. The corresponding FRG scale is referred to as the critical scale Λ_c . In BCS or spin-density-wave mean-field theory, in the weak-coupling limit at a constant density of states, the band gap equals the critical temperature up to a prefactor of the order of unity. In analogy to this observation, we expect the critical scale Λ_c to correspond to a critical temperature up to a factor of unity and therefore to

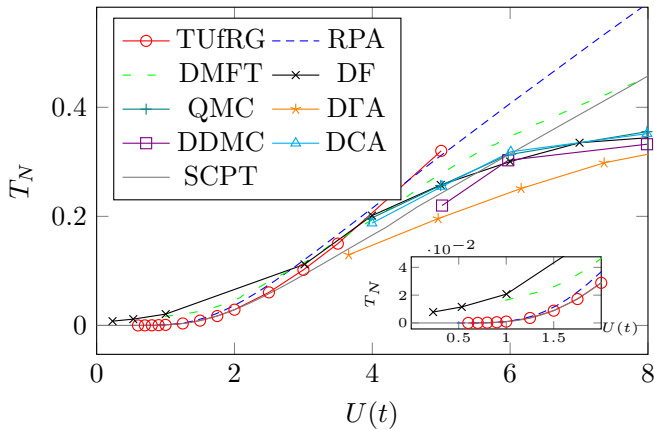


FIG. 3. Phase diagram of the three-dimensional Hubbard model. Presented is the critical scale Λ_c for the TUFGRG calculation in comparison with the critical temperature for previous calculations. For small interaction strengths the ordering energy scale obtained by FRG compares well with that obtained by other methods.

be comparable with literature values for critical temperatures. We point out that this stability analysis is not sensitive to first-order transitions. This is a known deficit that can be fixed with counterterm techniques [35]. However, admittedly, these are beyond the current numerical possibilities for general 2D and three-dimensional (3D) models.

IV. RESULTS

A. Results at half-filling

First, we run the 3D TUFGRG for the half-filled, fully nested Fermi surface for varying initial U . This results in a flow to strong coupling with leading Antiferromagnetic spin-density wave (AFM-SDW) correlations at a critical scale $\Lambda_c(U)$. This critical scale is shown in Fig. 3 in comparison to the critical temperatures obtained by RPA [3,36], self-consistent perturbation theory (SCPT) [6], dynamical mean field theory (DMFT) [11], dynamical cluster approximation (DCA) [12], quantum Monte Carlo (QMC) [9], determinantal diagrammatic Monte Carlo (DDMC) [13], dynamical vertex approximation (DGA) [14], and dual fermions (DF) [11]. Note that the RPA values are taken to be the renormalized critical temperatures according to Ref. [5], obtained by the Stoner criterion with the bare particle-hole bubble and by dividing the obtained T_N by 3 as a cheap way to account for corrections due to the local pairing channel [37]. In the limit of weak interactions $U \rightarrow 0$ the SCPT provides an analytical exact expression for the Néel temperature as described in Ref. [6]. Focusing on the shape of the $\Lambda_c(U)$ curve, it can be observed that our TUFGRG results in $D = 3$ in general compare reasonably well with the other methods at small interactions $U/t \lesssim 4$ even though the FRG scheme here does not take into account effects of the electronic self-energy and frequency dependence of the effective interactions. Clearly, the present FRG completely misses the plateau in T_c observed with other methods for $U/t \approx 8-10$. This failure is expected, as self-energy effects and higher-order vertices are neglected and, therefore, strong-coupling physics like pseudogap, Mott

transition, or local moment formation cannot be captured. Focusing on the quantitative comparison with renormalized RPA, the exact SCPT, and the dual-fermion data at $U/t \leq 4$, we can state the following. The FRG may have a lower critical scale than the RPA because the FRG includes the suppression of the magnetic channel by the full pairing channel and not only the local contribution [5,37]. In addition there may be competing effects from the direct particle-hole channel. While the TUFGRG curve starts to deviate from the RPA curve at $U \approx 1t$, it agrees well with the curve from SCPT up to $U \approx 2.5t$. The dual-fermion approach of Ref. [11] employs the ladder approximation; that is, it is something like RPA with local self-energy corrections and quite similar to single-site DMFT at weak U [11]. As the self-energy effects can be expected to be quite small at these U , it is no surprise that the critical temperatures are closer to the RPA values for intermediate U . We do not have a theory about why the DF and DMFT values are significantly higher than the RPA values in the limit $U \rightarrow 0$, but one might speculate that the on-site-repulsion screening in the particle-particle channel, which is captured as well in these approaches on the level of the impurity problem, is, for weak U , not as effective as in the renormalized RPA scheme on the extended lattice. For the interpretation of the TUFGRG ordering scales one should keep in mind that neglecting dynamic and self-energy effects is known to lead to slightly higher critical scales for the AFM-SDW instability, at least for 2D systems [31]. So our TUFGRG curve should be considered an upper estimate when channel coupling is included.

Beyond the question of the ordering energy scale, the TUFGRG contains information about the relative strength of the individual interaction channels. In Fig. 4 we show the full vertex in the C (spin) and P (pairing) channels, V_{ij}^C and V_{ij}^P , respectively, for the different form factors $i = j$ at the critical scale along the high-symmetry axes at $U = 1$. The contributions of combinations $i \neq j$ are always close to zero and therefore are not further considered here. The C channel exhibits a repulsive divergence for a momentum transfer of $R = (\pi, \pi, \pi)$ in the (on-site) s -wave form factor, exceeding the threshold V_{\max} . On the real-space lattice, the s -wave form factor means that the spin operators which order and which are built from bilinears in fermion operators are on site; that is, creation and annihilation operators have the same site index. The momentum transfer in the C channel with the peak at $R = (\pi, \pi, \pi)$ is characteristic of antiferromagnetic order, such that a corresponding phase transition is expected to occur at temperatures equal (up to factors of orders of unity) to the energy scale. The contributions of all other form factors to the C channel, shown in the inset of Fig. 4, are three orders of magnitude smaller, varying along the high-symmetry lines according to their momentum space shape. The P-channel vertex in Fig. 4 shows a dip of the s -wave form factor contribution at Γ which is still repulsive. This is the standard suppression of repulsive interactions in this channel. Again, the (on-site) s -wave form-factor contribution is three orders of magnitude larger than those of the other form factors. Figure 5 shows the P and C channels at the cutoff scale Λ_c for the system with a higher initial interaction of $U = 4t$. The characteristic features, i.e., the peaks in the C channel at R and in the P channel at Γ , are the same as in the $U = 1$ case. However, due

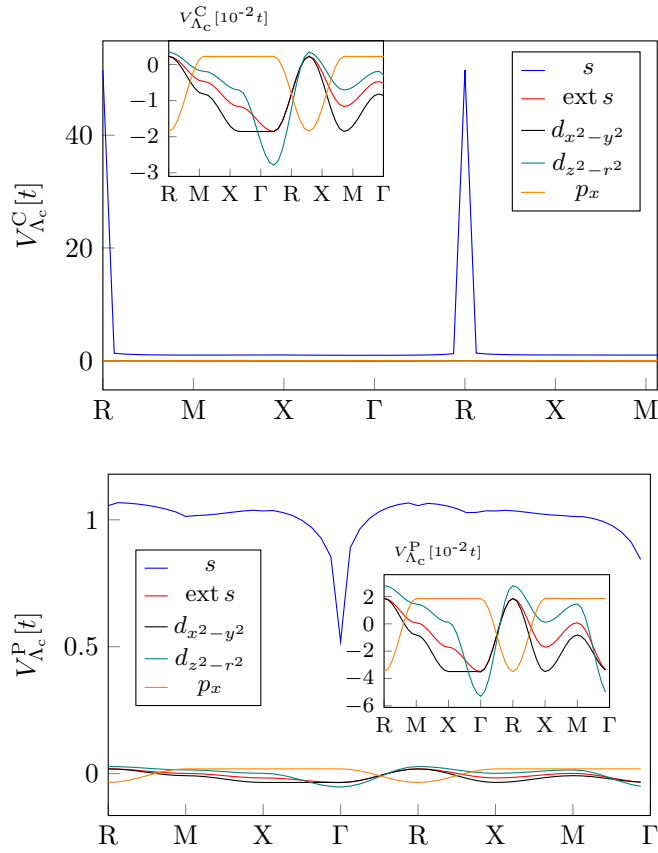


FIG. 4. Full vertex projected to the C channel (top) and P channel (bottom) at the critical scale depending on main momentum transfer t or s , respectively, moving along the high-symmetry lines for different form factors with an initial interaction of $U = 1t$.

to the larger initial interaction, there is a broader interaction background of $U \approx 4t$ in the s -wave form factor. This drives the interaction in the other form-factor representations, which develop more pronounced features corresponding to their set of form factors in most cases.

These results at half-filling can be understood as a first sanity check for the 3D TUFGR scheme. The expected AFM-SDW instability is reproduced, and quite a few details about the wave-vector structure of the effective interaction can be extracted. Regarding the numbers, the method's quantitative performance seems reasonable in the weak-coupling region for $U \leq \text{bandwidth}/3$, even if self-energy effects and frequency dependences of the vertices are neglected. This is valuable information for more complicated cases, where benchmarks are absent.

B. Results away from half-filling

The occurrence of unconventional pairing in the Hubbard model was subject to theoretical research already before the advent of quasi-2D cuprate high-temperature superconductors. In the mid-1980s, Scalapino and collaborators [17] investigated the doped 3D Hubbard model in spin-fluctuation theory and determined the leading pairing instabilities. Besides the AFM state close to half-filling they detected pairing channels corresponding to nearest-neighbor pairs as well as

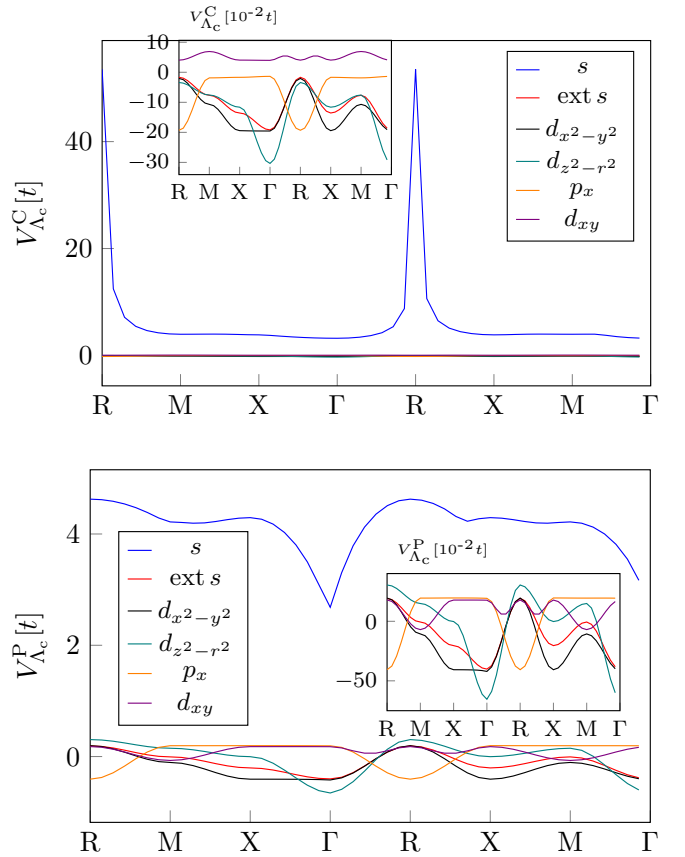


FIG. 5. Full vertex projected to the C channel (top) and P channel (bottom) at the critical scale depending on main momentum transfer moving along the high-symmetry lines for different form factors with an initial interaction of $U = 4t$.

pairing tendencies with some second-nearest-neighbor form factors like $d_{xy} \sim \sin(k_x)\sin(k_y)$. Hence, we perform the calculations away from half-filling by using the extended set of form factors corresponding to on-site, nearest, and next-nearest neighbors in Table I. For these calculations the vertex was represented by a 14^3 momentum grid, while the propagator bubble was evaluated on a 490^3 grid. If the system is hole doped away from half-filling, the critical scale decreases, as shown in Fig. 6. The momentum resolution, limited by computing resources, prohibits statements of critical scales lower than $\approx 10^{-5}$, such that the flow ended due to this criterion and not by the divergence of the vertex for $\mu \lesssim -1.0t$. In Fig. 6, the μ region where the flow did not diverge within the observable range is marked by a horizontal dashed line. However, from the observation of the flows in these cases educated guesses on the dominating orders at even lower scales are still possible.

For $\mu \gtrsim -0.5t$ we still observe a transition to an AFM state with a contribution of the vertex similar to those in the preceding section. As the doping moves the Fermi surface away from perfect nesting, the AFM state becomes incommensurate, and the critical scale for the runaway flow decreases. In Fig. 7 (top row) we show a cut along the $z = \pi$ plane of the C channel in the leading on-site form factor for both $\mu = 0t$ and $\mu = -0.4t$. The plots clearly show that the

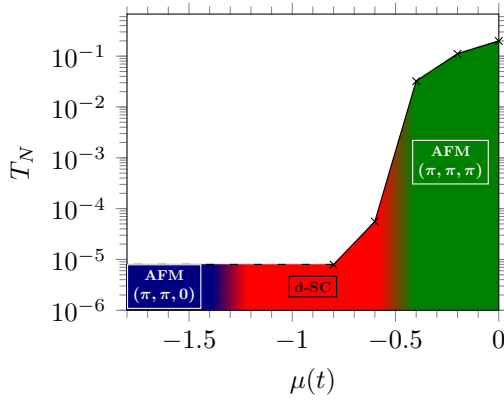


FIG. 6. Tentative TUFGR phase diagram of the doped 3D Hubbard model. Close to $\mu = 0.0t$ we observe AFM ordering with (π, π, π) ordering; around $\mu = -0.5t$ the ground state becomes $d_{z^2-r^2}$ superconducting, and around $\mu = -1.3t$ we observe predominant AFM tendencies, now with $(\pi, \pi, 0)$ ordering (or symmetry-related vectors). Below $\mu = -1.0t$ the flow does not diverge within a range down to $\Lambda_c = 8 \times 10^{-6}$; hence, the plotted line becomes flat. The resulting ordering tendencies are obtained from investigations of the flow and vertex at the smallest Λ .

AFM nesting becomes incommensurate, as the peak splits and moves slightly along (x, π, π) and (π, y, π) towards both M points on this plane. This split to a different set of nestings then causes the drop in critical scale.

For $-1.0t \lesssim \mu \lesssim -0.5t$ we observe a leading instability in the pairing channel, with a critical scale of the order of $\approx 10^{-5}$. A transition between the AFM and d -wave states is predicted from diagrammatic calculations [17] to happen at $\mu = -0.8t$, slightly below our values. Therefore, the inter-channel couplings present in our calculations but not in the previous spin-fluctuation theories seem to enlarge the d -wave regime. In this parameter region the leading instability occurs in the pairing channel with $d_{z^2-r^2}$ form factors at Γ , indicating a $d_{z^2-r^2}$ -superconducting phase (see Fig. 8). Of course, there are two more symmetry-related form factors with the same pairing strength that can be obtained from rotating the $d_{z^2-r^2}$ function to point along the x or y axis. These will then admix to the $d_{z^2-r^2}$ function the other basis function of this two-dimensional irreducible representation of O_h , customarily chosen as having $d_{x^2-y^2}$ symmetry. In Fig. 8 the basic feature of a divergence of the vertex in this form-factor basis can be seen, but with a much lower pairing strength. This disparity occurs presumably because the corresponding gap function would have longer nodal lines on the Fermi surface than the $d_{z^2-r^2}$ function. Regarding the C channel in this region, there is still a subdominant incommensurate AFM ordering tendency which continues the trend of peaks moving from R towards M (see Fig. 7).

To study the leading order in the region of $\mu \lesssim -1.0t$ we considered the change in the propagators P, C, and D as well as the vertex at $\Lambda = 10^{-5}$, where we ended the flow. For $\mu = -1.2t$ the leading contribution to the flow and the signature in the vertex still correspond to a $d_{z^2-r^2}$ -superconductivity (SC) phase. However, for even smaller μ the main contribution to the flow comes from the C channel. The vertex for this scale shows a peak close to $M = (\pi, \pi, 0)$; that is, the system tends

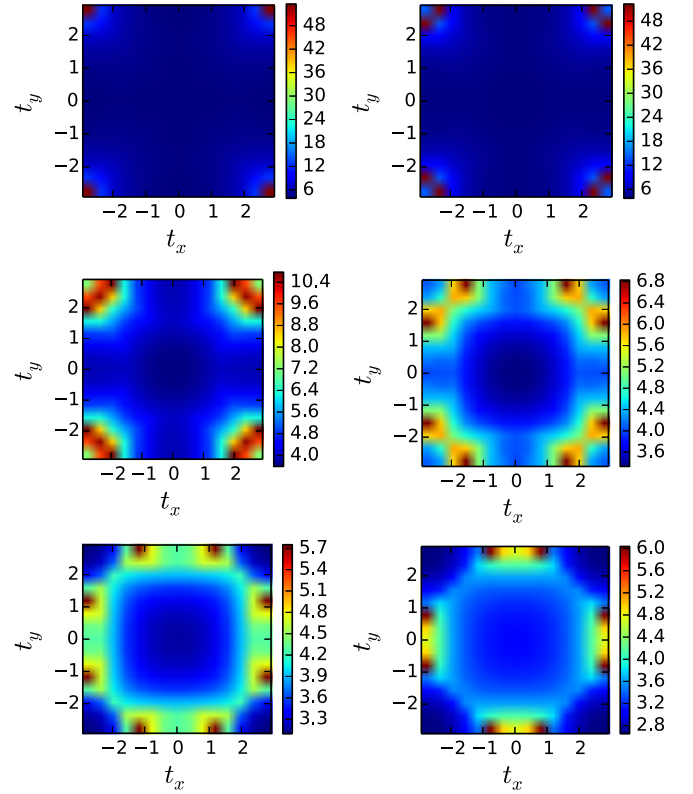


FIG. 7. Cut in the $z = \pi$ plane of the full vertex in the C channel with the on-site form factor at $U = 4t$ and $\mu = 0t, -0.4t, -0.6t, -1.0t, -1.4t, -1.8t$ from left to right and top to bottom.

to an antiferromagnetic order with in-plane ordering vector. Regarding the trend of increased doping for the AFM ordering peak, it moved from R in the undoped region towards M for $\mu \approx -2t$. Close to this chemical potential, the two incommensurate peaks corresponding to, e.g., $(\pi, \pi, \pm\eta)$, with η being a small positive number, get close to each other and thus strengthen the in-plane AFM tendency. This then destroys the d -SC order which still causes signatures in the vertex. As the Fermi surface of the 3D Hubbard model becomes an inflated octahedron at $\mu = -2.0t$ (see Fig. 2) with edges corresponding to a perfectly nested 2D square-lattice Fermi surface, a leading AFM order at the M points can be expected. Further investigations might also investigate the situation for even larger doping with μ below $-2.0t$.

V. CONCLUSION

We have applied the truncated-unity functional renormalization group to the three-dimensional Hubbard model. This study serves as a demonstration that this method allows us to investigate three-dimensional lattice-fermion models with functional renormalization group methods. Here we basically aimed to show that the scheme produces the correct physics and that it may even be used for quantitative questions.

At half band filling and perfect nesting we observed the well-known antiferromagnetic ground state of the 3D Hubbard model by analyzing the flow to strong coupling in the TUFGR. By using the TUFGR critical scale as an estimate

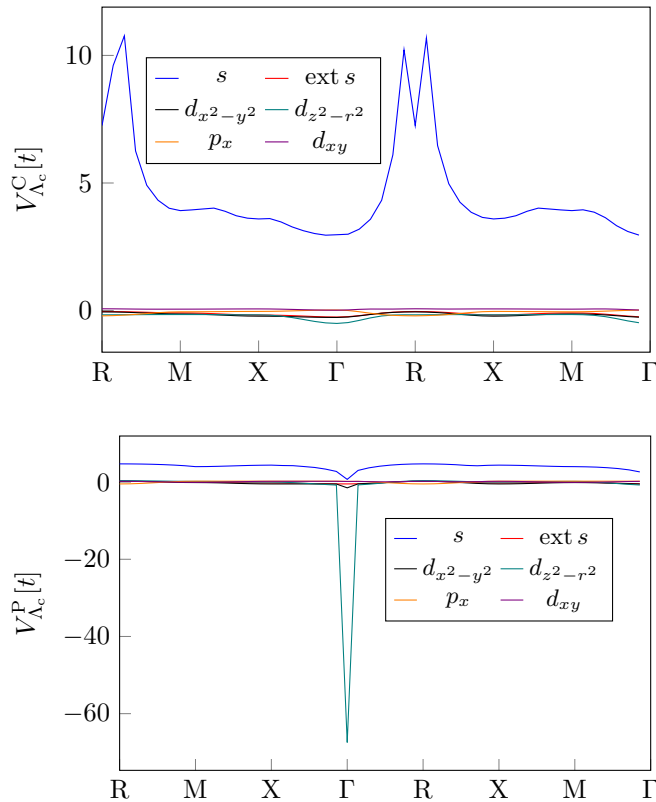


FIG. 8. Full TUFGRG vertex projected to the C channel (top) and P channel (bottom) at the critical scale depending on the main momentum transfer moving along the high-symmetry lines for different form factors with an initial interaction of $U = 4t$ and chemical potential $\mu = -0.6t$.

for the Néel ordering temperature T_N we could reasonably well reproduce the behavior of the $T_N(U)$ computed by other numerical techniques for weak coupling strengths $U \lesssim 4t$,

although we used a set of form factors limited to nearest neighbors. However, as expected, due to the approximations involved, our approach does not reproduce the plateau of T_N at intermediate coupling strength and the crossover to a decreasing ordering scale $\sim 1/U$ at larger U . Electron or hole doping of the system leads to a significant decrease of the critical scale as the Fermi surface does not provide perfect nesting anymore. For $\mu < -0.5$ the ground state becomes $d_{z^2-r^2}$ -wave superconducting, in good agreement with the predictions of Ref. [17]. For a doping towards $\mu \approx -2t$ this d -wave superconducting instability becomes suppressed by a tendency towards in-plane antiferromagnetic ordering. Further investigations of the doped 3D Hubbard model reducing the approximations are under way.

Due to the numerical advantages of the TUFGRG approach, the inclusion of self-energy feedback, frequency dependence, and, possibly, multiloop effects [31] is conceivable, potentially even in three dimensions after some well-chosen sacrifices. This will further increase the quantitative control of the method. It may also be interesting to analyze in more detail the critical behavior displayed by the TUFGRG and to understand to what extent nonfield behavior [14] can be reproduced depending on the approximation level. Furthermore, extensions to models with several orbitals should be feasible, with some necessary compromises in the momentum resolution.

ACKNOWLEDGMENTS

The authors gratefully acknowledge financial support through the DFG research training group 1995, DFG Grant No. HO-2422/12-1, and the computing time granted through JARA-HPC on the supercomputer JURECA at Forschungszentrum Jülich [38]. We thank D. Rohe, S. Andergassen, S. Blügel, C. Eckhardt, C. Hille, G. Schober, and A. Tagliavini for discussions.

-
- [1] E. H. Lieb and F. Y. Wu, *Phys. Rev. Lett.* **20**, 1445 (1968).
- [2] A. Georges and G. Kotliar, *Phys. Rev. B* **45**, 6479 (1992).
- [3] J. E. Hirsch, *Phys. Rev. B* **35**, 1851 (1987).
- [4] A. Martín-Rodero and F. Flores, *Phys. Rev. B* **45**, 13008 (1992).
- [5] J. K. Freericks and M. Jarrell, *Phys. Rev. Lett.* **74**, 186 (1995).
- [6] T. Schauerte and P. G. J. van Dongen, *Phys. Rev. B* **65**, 081105(R) (2002).
- [7] A. W. Sandvik, *Phys. Rev. Lett.* **80**, 5196 (1998).
- [8] I. Affleck, Z. Zou, T. Hsu, and P. W. Anderson, *Phys. Rev. B* **38**, 745 (1988).
- [9] R. Staudt, M. Dzierzawa, and A. Muramatsu, *Eur. Phys. J. B* **17**, 411 (2000).
- [10] S. Fuchs, E. Gull, M. Troyer, M. Jarrell, and T. Pruschke, *Phys. Rev. B* **83**, 235113 (2011).
- [11] D. Hirschmeier, H. Hafermann, E. Gull, A. I. Lichtenstein, and A. E. Antipov, *Phys. Rev. B* **92**, 144409 (2015).
- [12] P. R. C. Kent, M. Jarrell, T. A. Maier, and T. Pruschke, *Phys. Rev. B* **72**, 060411(R) (2005).
- [13] E. Kozik, E. Burovski, V. W. Scarola, and M. Troyer, *Phys. Rev. B* **87**, 205102 (2013).
- [14] G. Rohringer, A. Toschi, A. Katanin, and K. Held, *Phys. Rev. Lett.* **107**, 256402 (2011).
- [15] P. G. J. van Dongen, *Phys. Rev. Lett.* **67**, 757 (1991).
- [16] P. G. J. van Dongen, *Phys. Rev. B* **50**, 14016 (1994).
- [17] D. J. Scalapino, E. Loh, and J. E. Hirsch, *Phys. Rev. B* **34**, 8190 (1986).
- [18] P. Kopietz, L. Bartosch, and F. Schütz, *Introduction to the Functional Renormalization Group*, Lecture Notes in Physics Vol. 789 (Springer, Berlin, 2010).
- [19] W. Metzner, M. Salmhofer, C. Honerkamp, V. Meden, and K. Schönhammer, *Rev. Mod. Phys.* **84**, 299 (2012).
- [20] C. Platt, W. Hanke, and R. Thomale, *Adv. Phys.* **62**, 453 (2013).
- [21] C. Husemann and M. Salmhofer, *Phys. Rev. B* **79**, 195125 (2009).
- [22] C. Husemann, K.-U. Giering, and M. Salmhofer, *Phys. Rev. B* **85**, 075121 (2012).
- [23] A. Eberlein, *Phys. Rev. B* **92**, 235146 (2015).

- [24] W.-S. Wang, Y.-Y. Xiang, Q.-H. Wang, F. Wang, F. Yang, and D.-H. Lee, *Phys. Rev. B* **85**, 035414 (2012).
- [25] W.-S. Wang, Z.-Z. Li, Y.-Y. Xiang, and Q.-H. Wang, *Phys. Rev. B* **87**, 115135 (2013).
- [26] J. Lichtenstein, D. S. de la Peña, D. Rohe, E. D. Napoli, C. Honerkamp, and S. Maier, *Comput. Phys. Commun.* **213**, 100 (2017).
- [27] G. A. H. Schober, J. Ehrlich, T. Reckling, and C. Honerkamp, *Front. Phys.* **6**, 32 (2018).
- [28] D. S. de la Peña, J. Lichtenstein, and C. Honerkamp, *Phys. Rev. B* **95**, 085143 (2017).
- [29] N. Wentzell, G. Li, A. Tagliavini, C. Taranto, G. Rohringer, K. Held, A. Toschi, and S. Andergassen, *Phys. Rev. B* **102**, 085106 (2020).
- [30] D. Vilardi, C. Taranto, and W. Metzner, *Phys. Rev. B* **96**, 235110 (2017).
- [31] A. Tagliavini, C. Hille, F. B. Kugler, S. Andergassen, A. Toschi, and C. Honerkamp, *Sci. Post. Phys.* **6**, 9 (2019).
- [32] C. Hille, D. Rohe, C. Honerkamp, and S. Andergassen, *Phys. Rev. Res.* **2**, 033068 (2020).
- [33] M. Salmhofer and C. Honerkamp, *Prog. Theor. Phys.* **105**, 1 (2001).
- [34] F. B. Kugler and J. von Delft, *Phys. Rev. Lett.* **120**, 057403 (2018).
- [35] R. Gersch, J. Reiss, and C. Honerkamp, *New J. Phys.* **8**, 320 (2006).
- [36] R. T. Scalettar, D. J. Scalapino, R. L. Sugar, and D. Toussaint, *Phys. Rev. B* **39**, 4711 (1989).
- [37] J. Kanamori, *Prog. Theor. Phys.* **30**, 275 (1963).
- [38] Jülich Supercomputing Centre, *J. Large-Scale Res. Facil.* **4**, A132 (2018).